MAR Analysis of a Spherical-Circular Printed Antenna With Finite Ground Excited by an Axially Symmetric Probe

Sébastien Rondineau, Alexander I. Nosich, *Senior Member, IEEE*, Jean-Pierre Daniel, Mohamed Himdi, and Sergei S. Vinogradov

***Abstract*—The paper deals with an accurate mathematical and numerical analysis of a spherical-circular antenna printed over a coaxial spherical-circular ground conductor. A coaxial probe simulated by a radial driving current placed between two conductors excites the antenna. Consideration is done in terms of the spherical vector wave function expansions of the field in each partial domain. The problem is cast into a coupled set of the dual-series equations for the expansion coefficients, and then to an infinite-matrix equation having favorable features. This is achieved by following the *Method of Analytical Regularization* developed earlier for the analysis of spherical reflectors.**

***Index Terms*—Analytical regularization, spherical disk, conformal microstrip antenna, far-field radiation.**

I. Introduction

A GROWING interest is observed in the patch antennas conformally printed on spherical surfaces. The reason can be seen in potential applications to the cellular and indoor-communication base stations, and in mobile terminals. Indeed, these antennas offer a designer a higher degree of freedom than flat structures. At first, a simple "cavity-model" analysis was published on the spherical-circular microstrip antenna (MSA) [1] shaped as a perfectly electrically conducting (PEC) spherical disk placed on the outer surface of a spherical dielectric layer backed with a PEC spherical ground. Superstrate-covered spherical-circular MSA was studied in [2]. Later on, annular-ring and combined circular plus annular-ring MSA with the spherical ground conductors were considered [3], [4]. Book [5] summarized the state-of-the-art achieved by 1999. The treatment was usually based on a moment method (MM) version, with so-called "cavity modes" frequently taken as expansion basis. Recently, finite-difference time-domain (FDTD) method has come into wide utilization. Due to its versatility, this method is normally found behind many commercially available printed-antenna simulators, many of which boast of applicability to curved substrates as well.

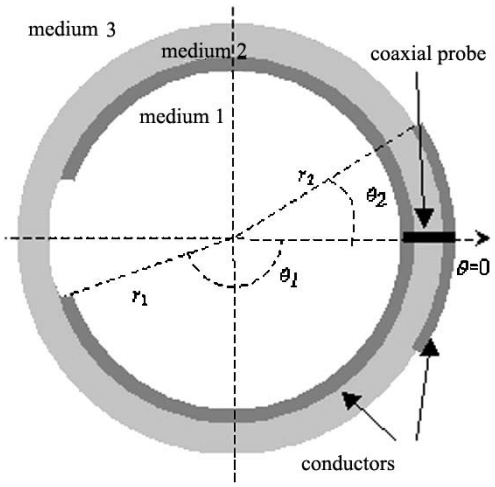

Fig. 1. Cross-sectional view of the rotationally symmetric two-conductor conformal antenna printed on a spherical substrate and fed by a centered coaxial probe.

However, conventional numerical methods result in very large matrix equations and need very high memory capacity and computation time. Therefore, it is not a surprise that none of the published analyzes show frequency dependence of major MSA characteristics in a wide band. Moreover, these methods do not guarantee a convergence because of ill-conditioned matrices, numerical instabilities, and vulnerability to high-Q resonances [6], [7]. Therefore, a technique able to ensure fast and uniform point-wise convergence of the solution and has controlled computational error is still attractive. The Method of Analytical Regularization, or MAR [8], sometimes-called semi-inversion method shows a way to achieve these goals. Generally, MAR converts a first-kind singular integral equation to a well-conditioned second-kind matrix equation with the dominant main diagonal, and therefore serves as analytical preconditioner of originally ill-posed problem. Then both numerical convergence and efficiency are achieved and the error is controlled by the matrix truncation.

A spherical-circular MSA was treated with MAR in [9] assuming its axially symmetric excitation by a radial electric dipole (RED). Here, the MAR was based on the technique previously developed in the acoustic and electromagnetic wave scattering by spherical disks in free-space environment

Manuscript received January 14, 2002; revised June 16, 2003.

S. Rondineau was with IETR, UMR-CNRS 6164, Université de Rennes 1, Rennes Cédex 35042, France. He is now with the Microwave and Active Antenna Laboratory of the Electrical and Computer Engineering Department, University of Colorado, Boulder, CO 80309-0425 USA (e-mail: sebastien@nemes.colorado.edu).

A. I. Nosich is with the Institute of Radio-Physics and Electronics of the National Academy of Sciences of Ukraine, Kharkov 61085, Ukraine (e-mail: alex@emt.kharkov.ua).

J.-P. Daniel and M. Himdi are with IETR, UMR-CNRS 6164, Université de Rennes 1, Rennes Cédex 35042, France (e-mail: jean-pierre.daniel@univ-rennes1.fr; mohamed.himdi@univ-rennes1.fr).

S. S. Vinogradov is with the Department of Mathematics, University of Dundee, DD1 4HN, Scotland, U.K. (e-mail:svinogra@maths.dundee.ac.uk).

Digital Object Identifier 10.1109/TAP.2004.827254

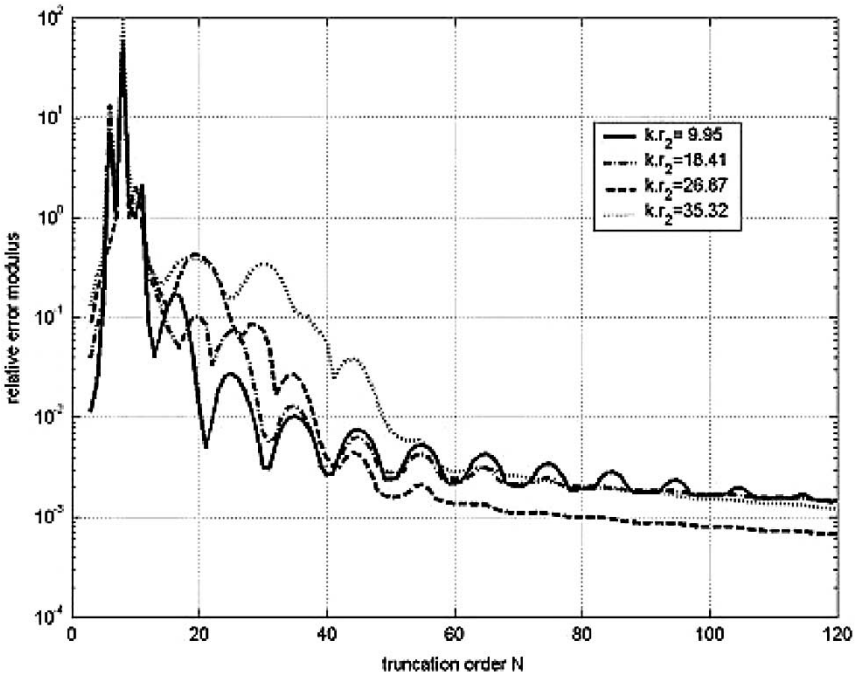

Fig. 2. Relative computational error versus the order of matrix truncation for various normalized frequencies. $\theta_1 = 180°, \theta_2 = 18°, r_1/r_2 = 0.97, \varepsilon_{r1} = \varepsilon_{r3} = 1, \varepsilon_{r2} = 1.3$.

[10]–[13]. This technique avoids formulating integral equations and starts from introducing the Debye potentials—auxiliary functions satisfying the Helmholtz equation. Expanding these potentials in terms of the Legendre functions in spherical domains and using the boundary conditions leads to the dual-series equations (DSEs). They are further decomposed into the static and dynamic parts, and the former is inverted analytically thanks to the properties of the Abel integral representations for the Legendre functions. Such a procedure results in the *regularization*: unknowns are found as a solution to the Fredholm second-kind matrix equation.

In this paper, MAR is applied to a conformal printed antenna containing two finite-size spherical-circular disk conductors conformally placed at the interfaces of a layered dielectric sphere and fed by a coaxial probe. For convenience, we shall refer to the inner conductor as ground, and to the outer one as patch, however this terminology can be reversed. The both conductors have a common axis of rotational symmetry and the probe is assumed to be on the symmetry axis as well. Hence, our antenna geometry is a generalization of a simple spherical-circular MSA considered in [9]. Although disk MSA is frequently used with the broadside radiation, centered radial-probe excitation can generate only an axisymmetric radiation pattern. Such omnidirectional, in the horizontal plane, patterns are necessary in the mobile communications [14], radio LAN [15], and broadband distribution systems [16]. Variable size of the ground provides an additional degree of freedom in the antenna design. The basic steps in the solution are similar to that of [9] but differ in the way of presenting the fields: instead of the Debye potentials we use a more up-to-date technique of the spherical vector wave functions. Of course, the presence of the second spherical-disk conductor entails numerous complications: instead of a single set of DSE, here we obtain a coupled pair of sets; the far field depends on the currents induced on the both conductors, etc.

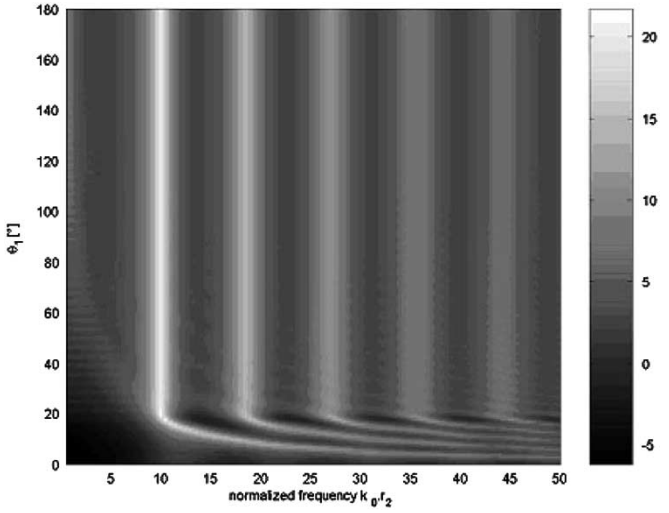

Fig. 3. Relief of the total radiated power normalized to the power radiated by the feed alone, on the plane $k_0 r_2 - \theta_1$. $\theta_2 = 18°, r_1/r_2 = 0.97, \varepsilon_{r1} = \varepsilon_{r3} = 1, \varepsilon_{r2} = 1.3$.

The rest of the paper is organized as follows. Section II contains the problem formulation and the derivation of the DSE. Section III deals with the analytical regularization of DSE by extracting the disk-in-free-space parts and inverting their static limits. In Section IV, we derive the formulas for the currents, and far-field antenna characteristics. Section V contains a review of numerical results showing the effect of the finite-size ground surface and the curvature. Experimental verification of the obtained results is briefly outlined in Section VI. The conclusions are summarized in Section VII. The study is done with the $e^{+j\omega t}$ time-harmonic dependence (ω is the angular frequency).

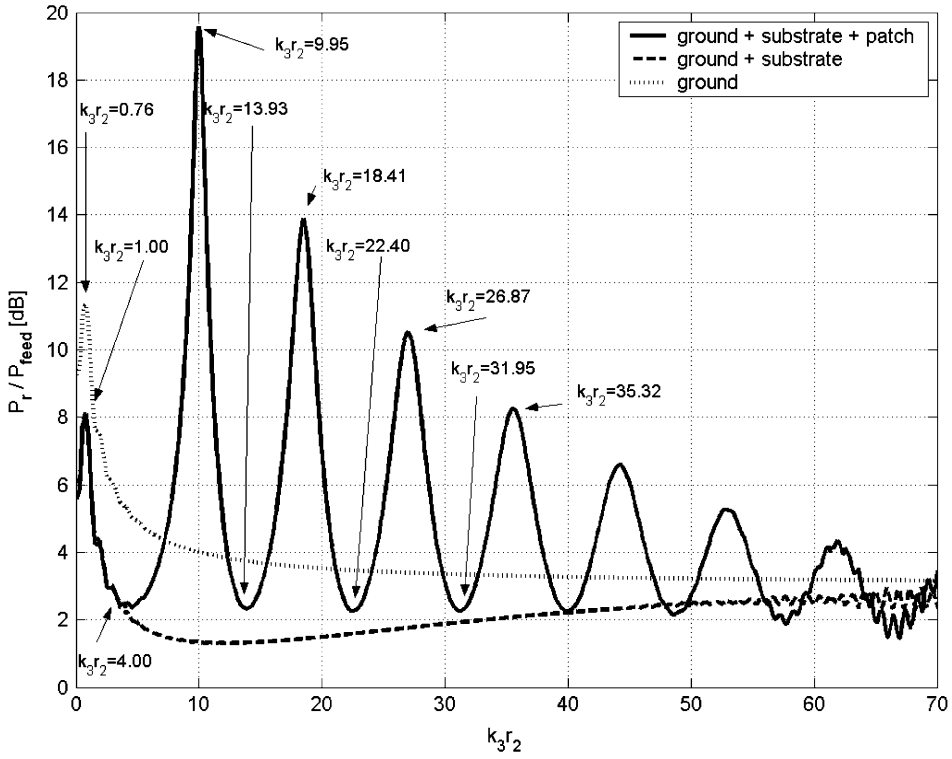

Fig. 4. Total radiated power normalized to the feed radiated power. $\theta_1 = 160°, \theta_2 = 18°$ in the case of the presence of the patch and 0° otherwise, $r_1/r_2 = 0.97, \varepsilon_{r1} = \varepsilon_{r3} = 1, \varepsilon_{r2} = 1.3$ in the case of the presence of the substrate and 1.0 otherwise.

II. Formulation and Basic Equations

A. Antenna Geometry

The considered antenna structure is shown in Fig. 1. A two-layer dielectric sphere has the inner and outer interface radii r_1 and r_2, and the relative permittivities of the layers are ε_1 and ε_2, respectively. Surrounding medium is free space. Between the layers, a PEC spherical disk of the angular size θ_1 is placed. This is the ground conductor. On the outer surface of the dielectric sphere, another PEC spherical disk of the angular size θ_2 is placed. This is the patch. A coaxial probe simulated by a radial driving current between two conductor centers feeds the antenna. The disks are assumed infinitely thin. Note that both conductors have angular sizes varying from 0 to π that enables us to include into single formulation the previously studied cases of a RED exciting a dielectric-coated PEC sphere, and a spherical-disk MSA with complete sphere as a ground conductor.

B. Electromagnetic Model

The chosen feed is a centered coaxial probe whose current is oriented along the radius with the fixed amplitude I_0

$$\vec{J}^e(r,\theta,\varphi) = \frac{I_0}{r^2 \sin\theta} 1(r_1, r_2)\delta(\theta)\delta(\varphi)\vec{r}. \tag{1}$$

Here $\delta(\,\cdot\,)$ is the Dirac-delta distribution, $1(A)$ the unit function on the set A, and $\vec{r}$ the radial unit vector. Note that the driving current (1) is ϕ-independent. Placed in a homogeneous medium, such a current generates electromagnetic field whose nonzero components are as follows:

$$\vec{E} = E_r\vec{r} + E_\theta\vec{\theta}, \quad \vec{H} = H_\varphi\vec{\varphi} \tag{2}$$

where $\vec{\theta}$ and $\vec{\varphi}$ are the angular unit vectors. In our case current (1) is placed in the inhomogeneous but still φ-independent environment. Therefore, without going into details we can correctly guess that the total field of the studied MSA will have the same components (2) as the "incident" field.

Off the MSA boundaries, total field must solve the time-harmonic Maxwell equations with source given by (1), and satisfy a set of boundary conditions at the PEC elements and transmission conditions at the free parts of the dielectric surfaces. Besides, it must satisfy Silver–Muller radiation condition [17] as electromagnetic analog of the scalar Sommerfeld condition. This requires the far field, due to (2) and associated discussion, to behave in the following manner:

$$E_\theta(r,\theta) = \frac{1}{\eta_3} H_\varphi(r,\theta) = E_0 \frac{e^{-jk_3 r}}{k_3 r} f(\theta), E_r(r,\theta) = O(r^{-2}) \tag{3}$$

where it will be convenient to set $E_0 = (4\pi)^{-1} k_3 \eta_3 I_0$. Note that k and η are respectively the wave number and the intrinsic impedance of the considered medium.

Finally, edge condition follows from the demand that the power contained in any bounded volume V_0 of the space, is finite

$$\int_{V_0} (\varepsilon|\vec{E}|^2 + \mu|\vec{H}|^2)\, dV < \infty. \tag{4}$$

This condition determines the field behavior at the rims, namely, $E_r, E_\theta = O(\rho^{-1/2}), H_\varphi = O(\rho^{1/2})$, where $\rho \to 0$ is the distance to either of the disk rims in the plane (r,θ).

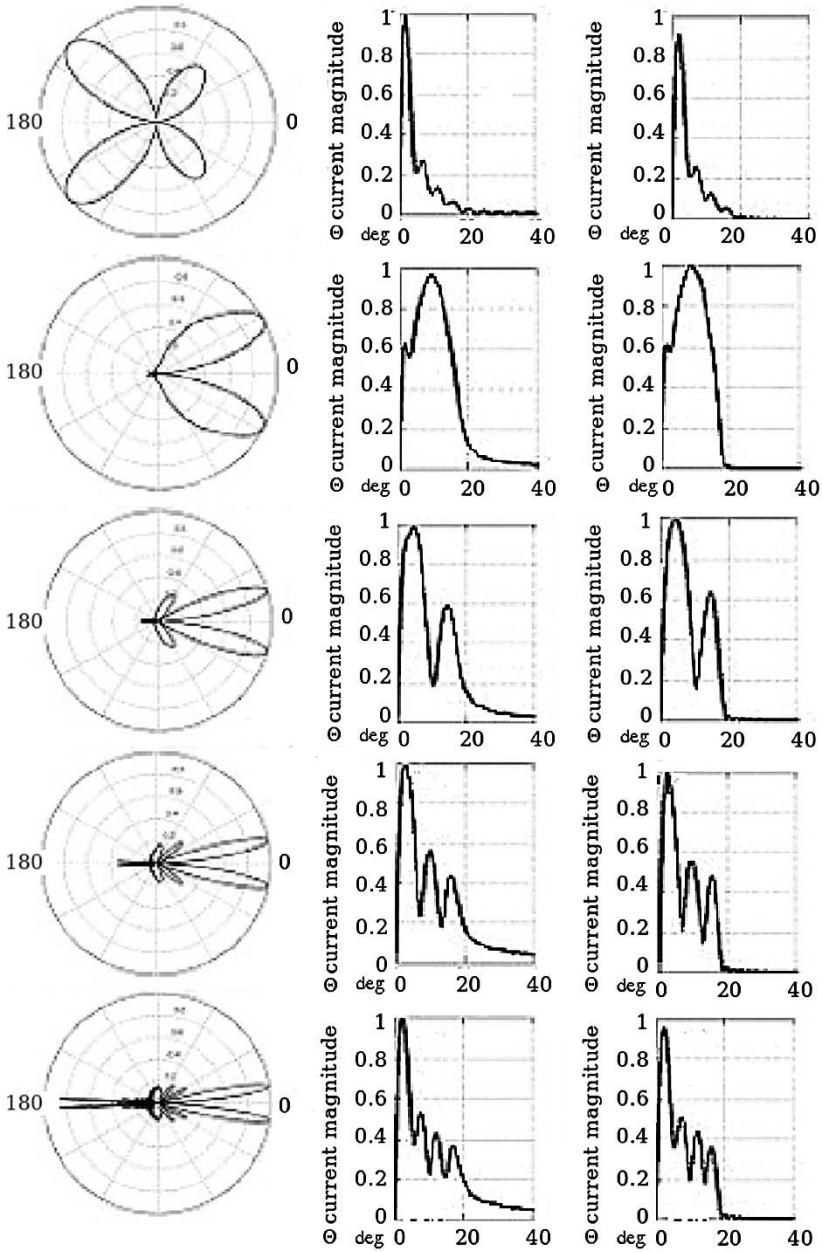

Fig. 5. Normalized far-field patterns (left column) and currents on the spherical disks (cap 1 at the middle column and cap 2 at the right one) in the maxima of the radiated power marked in Fig. 4. $\theta_1 = 160°, \theta_2 = 18°, r_1/r_2 = 0.97, \varepsilon_{r1} = \varepsilon_{r3} = 1, \varepsilon_{r2} = 1.3$. From top to bottom, the values of the normalized frequency are $kr_2 = 1.00, 9.95, 18.41, 26.87$, and 35.32.

Under these conditions, the problem of finding the total electromagnetic field may have only one solution (the uniqueness theorem). Now we shall work on developing a numerical scheme of approaching this solution as close as possible in terms of finite digit computations.

C. Field Expansions and Basic Equations

Because of the spherical geometry, it is natural to expand the electromagnetic field in terms of the spherical vector wave functions [18]. Such an expansion is found by solving the Maxwell equations for the electromagnetic field in the spherical coordinates and taking account of the rotational symmetry. For example, thanks to expression (1), the shape of the electromagnetic field of the feed in the homogeneous medium 2 is found to be

$$\vec{E}^i = E_0 \sum_{n=1}^{\infty} \sum_{s=1,4} \alpha_n^{\text{is}} \cdot \vec{N}_n^s, \vec{H}^i = \frac{jE_0}{\eta} \sum_{n=1}^{\infty} \sum_{s=1,4} \alpha_n^{\text{is}} \cdot \vec{M}_n^s \tag{5}$$

where the coefficients are given as follows:

$$\alpha_n^{i1}(r) = (2n+1) \int_r^{r_2} \frac{Z_n^4(k_2\rho)}{k_2\rho} d\rho,$$
$$\alpha_n^{i4}(r) = (2n+1) \int_{r_1}^{r} \frac{Z_n^1(k_2\rho)}{k_2\rho} d\rho \tag{6}$$

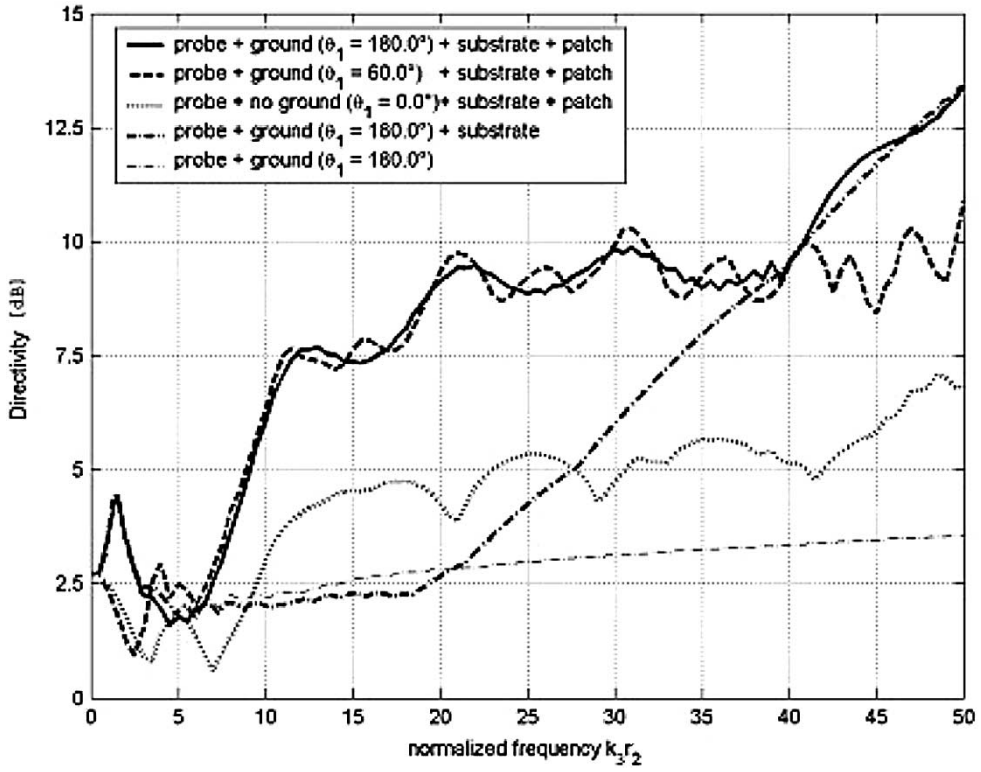

Fig. 6. Directivity associated with different ground sizes: $\theta_2 = 18°$ in the case of the presence of the patch and $\theta_2 = 0°$ otherwise, $r_1/r_2 = 0.97, \varepsilon_{r1} = \varepsilon_{r3} = 1, \varepsilon_{r2} = 1.3$ in the case of the presence of the substrate and $\varepsilon_{r2} = 1$ otherwise.

and the spherical modal vectors

$$\vec{M}_n^s = t_n^2 \cdot Z_n^s \cdot \hat{\varphi}, \quad \vec{N}_n^s = t_n^3 \cdot \frac{Z_n^s}{x} \cdot \hat{r} - t_n^2 \cdot K_n^s \cdot \hat{\theta} \tag{7}$$

Z_n^1 and Z_n^4 are the spherical Bessel function of the 1st kind and spherical Hankel function of the 2nd kind of the order n and argument $x = k_q r$, respectively. The other functions involved in (7) are

$$K_n^s(x) = \frac{1}{x}\frac{d}{dx}\left[x \cdot Z_n^s(x)\right] \tag{8}$$

$$t_n^2(\theta) = -P_n^1(\cos\theta), \quad t_n^3(\theta) = n(n+1) \cdot P_n(\cos\theta) \tag{9}$$

where $s = 1, 4$, and P_n^m represents the associated Legendre function of order m and degree n.

The PEC spherical disks are disturbing elements that cause a response to the given excitation, which is a radial probe. As both the feed field and the boundary, edge, and radiation conditions are ϕ-independent, no other field components besides those of the probe field appear in the secondary field. Therefore, it can be expanded in terms of the same vector spherical functions as the feed field

$$\vec{E}^q = E_0 \sum_{n=1}^{\infty} \sum_{s=1,4} \alpha_n^{\mathrm{sq}} \cdot \vec{N}_n^s, \vec{H}^q = \frac{jE_0}{\eta_q} \sum_{n=1}^{\infty} \sum_{s=1,4} \alpha_n^{\mathrm{sq}} \cdot \vec{M}_n^s \tag{10}$$

Here $q = 1, 2, 3$ is the number of the layer. Note that the spherical-wave coefficients are different for each q-th layer. Furthermore, some coefficients vanish in the most inner region ($q = 1$): $\alpha_n^{41} = 0$, and in the most outer region ($q = 3$): $\alpha_n^{13} = 0$.

D. Dual Series Equations

By applying the boundary and continuity conditions at $r = r_{1,2}$ to the electromagnetic field (10), we obtain the four equations in terms of the dual series

$$\sum_{n=1}^{\infty} \begin{Bmatrix} \alpha_n^{11} \\ \alpha_n^{43} \end{Bmatrix} \cdot \begin{Bmatrix} K_n^1(k_1 r_1) \\ K_n^4(k_3 r_2) \end{Bmatrix} \cdot P_n^1(\cos\theta) = 0, 0 \le \theta < \begin{Bmatrix} \theta_1 \\ \theta_2 \end{Bmatrix} \tag{11}$$

$$\sum_{n=1}^{\infty} \left[\begin{Bmatrix} \alpha_n^{11} \cdot u_n \\ \alpha_n^{43} \cdot v_n \end{Bmatrix} + \begin{Bmatrix} \alpha_n^{43} \cdot \tilde{\delta}_n \\ \alpha_n^{11} \cdot \tilde{\gamma}_n \end{Bmatrix} \right] P_n^1(\cos\theta) = \sum_{n=1}^{\infty} \left[\begin{Bmatrix} \beta_n^{i1} \cdot u_n^i \\ \beta_n^{i4} \cdot v_n^i \end{Bmatrix} + \begin{Bmatrix} \beta_n^{i4} \cdot \delta_n^i \\ \beta_n^{i1} \cdot \gamma_n^i \end{Bmatrix} \right] P_n^1(\cos\theta), \begin{Bmatrix} \theta_1 \\ \theta_2 \end{Bmatrix} < \theta \le \pi \tag{12}$$

where

$$u_n \cdot \eta_1 \cdot \eta_2 = \eta_2 \cdot Z_n^1(k_1 r_1) - \eta_1 \cdot K_n^1(k_1 r_1) \cdot R_n,$$
$$v_n \cdot \eta_2 \cdot \eta_3 = \eta_2 \cdot Z_n^4(k_3 r_2) - \eta_3 \cdot K_n^4(k_3 r_2) \cdot S_n \tag{13}$$

$$u_n^i \cdot \eta_2 = Z_n^1(k_2 r_1) - K_n^1(k_2 r_1) \cdot R_n,$$
$$v_n^i \cdot \eta_2 = Z_n^4(k_2 r_2) - K_n^4(k_2 r_2) \cdot S_n \tag{14}$$

$$\tilde{\gamma}_n = jK_n^1(k_1 r_1)/\eta_2 \Delta_n (k_2 r_2)^2,$$
$$\tilde{\delta}_n = -jK_n^4(k_3 r_2)/\eta_2 \Delta_n (k_2 r_1)^2 \tag{15}$$

$$\gamma_n^i = jK_n^1(k_2 r_1)/\eta_2 \Delta_n (k_2 r_2)^2$$
$$\delta_n^i = -jK_n^4(k_2 r_2)/\eta_2 \Delta_n (k_2 r_1)^2 \tag{16}$$

$$R_n \Delta_n = K_n^4(k_2 r_2) \cdot Z_n^1(k_2 r_1) - Z_n^4(k_2 r_1) \cdot K_n^1(k_2 r_2),$$
$$S_n \Delta_n = Z_n^4(k_2 r_2) K_n^1(k_2 r_1) - Z_n^1(k_2 r_2) K_n^4(k_2 r_1) \tag{17}$$

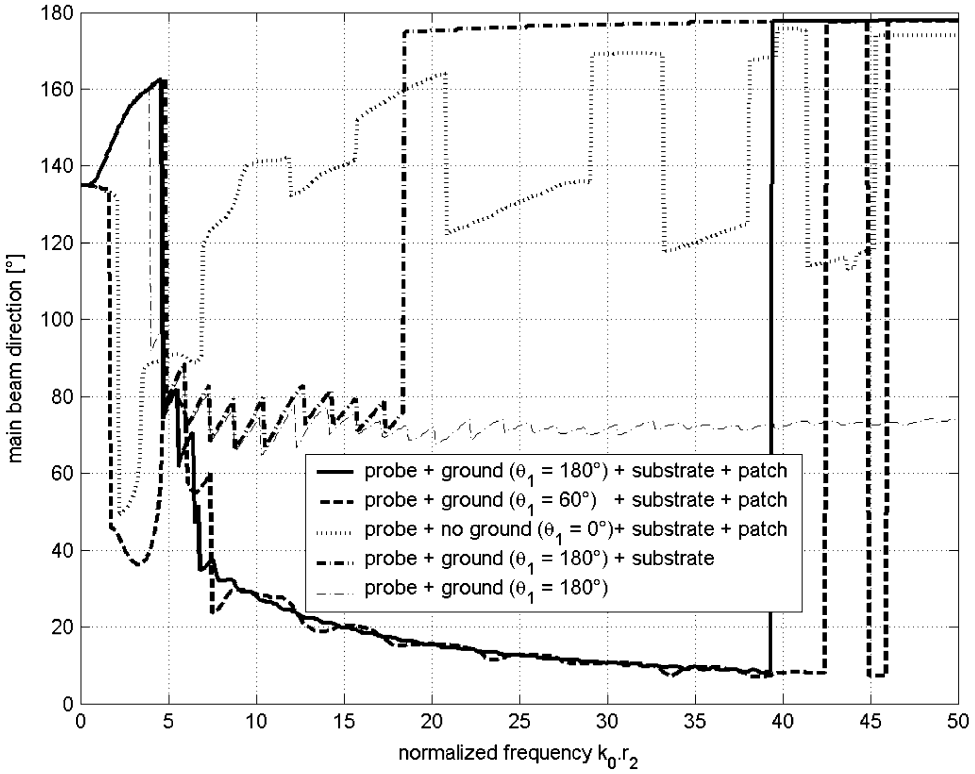

Fig. 7. Direction of the main beam associated with different ground sizes. $\theta_2 = 18°$ in the case of the presence of the patch and $\theta_2 = 0°$ otherwise, $r_1/r_2 = 0.97, \varepsilon_{r1} = \varepsilon_{r3} = 1, \varepsilon_{r2} = 1.3$ in the case of the presence of the substrate and $\varepsilon_{r2} = 1$ otherwise.

$$\Delta_n = K_n^4(k_2r_2)\cdot K_n^1(k_2r_1) - K_n^1(k_2r_2)\cdot K_n^4(k_2r_1),$$
$$\beta_n^{i1,4} = \alpha_n^{i1,4}(r_{2,1}) \tag{18}$$

E. Class of Expansion Coefficients

The following orthogonality property holds at the surface of the unit sphere:

$$\oint\int_S \vec{N}_n^s \cdot \vec{N}_{n'}^{s*}\, d\Omega = 4\pi n^2 \frac{(n+1)^2}{2n+1}\delta_{nn'}\left(\left|\frac{Z_n^s(x)}{x}\right|^2 + \frac{|K_n^s(x)|^2}{n(n+1)}\right)$$
$$\oint\int_S \vec{M}_n^s \cdot \vec{M}_{n'}^{s*}\, d\Omega = 4\pi n \frac{n+1}{2n+1}\delta_{nn'}\left|Z_n^s(x)\right|^2 \tag{19}$$

where z^* means the complex conjugate of z. Therefore, the edge condition (4), being applied to the interior spherical volume $r < r_1$ and to the spherical layer $r_2 < r < \text{const}$ leads to the requests that

$$\sum_{n=1}^{\infty} \left|n \cdot K_n^s(k_q r_p)\right|^2 \left|\alpha_n^{\text{sq}}\right|^2 < \infty \tag{20}$$

where $s = 1, 4, q = 1, 3$, and $p = 1, 2$.

III. Analytical Regularization

In order to follow the MAR scheme in solving DSE (11) and (12), it is convenient to change unknowns to x_n^1 and x_n^2

$$x_n^1 = n\frac{n+1}{2n+1}a_n^{11}u_n, \quad x_n^2 = n\frac{n+1}{2n+1}a_n^{43}v_n \tag{21}$$

Then it is easy to see that

$$\alpha_n^{11}K_n^1(k_1r_1) = x_n^1\Omega_1\left(1 - g_n^1\right)$$
$$\alpha_n^{43}K_n^4(k_3r_2) = x_n^2\Omega_2\left(1 - g_n^2\right) \tag{22}$$

where, after some algebra

$$\Omega_1 = \frac{2\eta_1/k_1r_1}{1 + \frac{\eta_1}{\eta_2}\frac{k_2}{k_1}}, \quad \Omega_2 = \frac{-2\eta_3/k_3r_2}{1 + \frac{\eta_3}{\eta_2}\frac{k_2}{k_3}} \tag{23}$$

$$g_n^1 = 1 - \frac{2n+1}{n(n+1)}\frac{K_n^1(k_1r_1)}{\Omega_1 \cdot u_n}$$
$$g_n^2 = 1 - \frac{2n+1}{n(n+1)}\frac{K_n^4(k_3r_2)}{\Omega_2 \cdot v_n} \tag{24}$$

where $g_n^{1,2} = \text{O}(k_0r_1n^{-1}) + \text{O}(r_1^{2n}/r_2^{2n})$ if $n \to +\infty$, and $\Omega_{1,2}$ do not depend on n. Thanks to that, DSE (12), (13) become

$$\sum_{n=1}^{\infty} x_n^j\left(1 - g_n^j\right)P_n^1(\cos\theta) = 0, 0 \le \theta < \theta_j, \tag{25}$$

$$\sum_{n=1}^{\infty}(2n+1)\left[\frac{x_n^j + x_n^k\gamma_n^j}{n(n+1)} - p_n^j\right]P_n^1(\cos\theta) = 0, \quad \theta_j < \theta \le \pi \tag{26}$$

where $j=1,2, k=2,1$, and the following notations have been introduced:

$$p_n^1=\frac{\beta_n^{i1}u_n^i+\beta_n^{i4}\delta_n^i}{2n+1},\quad p_n^2=\frac{\beta_n^{i4}v_n^i+\beta_n^{i1}\gamma_n^i}{2n+1} \tag{27}$$

$$\gamma_n^1=\tilde{\gamma}_n u_n^{-1},\quad \gamma_n^2=\tilde{\delta}_n v_n^{-1} \tag{28}$$

It can be seen that $p_n^j,\gamma_n^j=\mathrm{O}(k_3^2r_1^2n^{-2})+\mathrm{O}(r_1^n/r_2^n)$ if $n\to\infty$. Besides, from (20) and (21) we conclude that the unknown coefficients must belong to the class determined by the inequalities

$$\sum_{n=1}^{\infty}\left|x_n^j\right|^2<\infty, j=1,2 \tag{29}$$

Now we assume a uniform convergence of (25) and integrate it in θ in term-by-term manner. On using the formula $P_n^1(\cos\theta)=\partial P_n(\cos\theta)/\partial\theta$, we obtain that

$$\sum_{n=1}^{\infty}x_n^j\left(1-g_n^j\right)\,P_n(\cos\theta)=C^j\,P_0(\cos\theta),\qquad 0\le\theta<\theta_j,\quad j=1,2 \tag{30}$$

where C^1 and C^2 are some constants to be determined. Now, the Mehler–Dirichlet formulas give integral representations of the Legendre polynomials and associated functions [19] that enable us to convert DSE to the following equations:

$$\int_0^{\theta}\left[C^j\cos\frac{\varphi}{2}-\sum_{n=1}^{\infty}x_n^j\left(1-g_n^j\right)\cos\frac{2n+1}{2}\varphi\right]\times\frac{d\varphi}{\sqrt{\cos\varphi-\cos\theta}}=0 \quad \text{for } 0\le\theta<\theta_j,\quad j=1,2,k=2,1 \tag{31}$$

$$\frac{\int_0^{\theta}\sum_{n=1}^{\infty}\left[x_n^j+x_n^k\gamma_n^j-n(n+1)p_n^j\right]\cos\left(\frac{2n+1}{2}\varphi\right)\,d\phi}{\sqrt{\cos\varphi-\cos\theta}}=0, \quad \text{for } \theta_j<\theta\le\pi, j=1,2,k=2,1 \tag{32}$$

Each of the above equations is a homogeneous integral equation of the Abel type. Then, each integrand function vanishes on the whole interval of the equation validity, hence

$$\sum_{n=1}^{\infty}x_n^j\cos\frac{2n+1}{2}\theta=C^j\cos\frac{\theta}{2}+\sum_{n=1}^{\infty}g_n^jx_n^j\cos\frac{2n+1}{2}\theta \quad \text{for } 0\le\theta<\theta_j,\quad j=1,2,k=2,1 \tag{33}$$

$$\sum_{n=1}^{\infty}x_n^j\cos\frac{2n+1}{2}\theta=\sum_{n=1}^{\infty}\left[n(n+1)p_n^j-x_n^k\gamma_n^k\right]\cos\frac{2n+1}{2}\theta \quad \text{for } \theta_j<\theta\le\pi,\quad j=1,2,k=2,1. \tag{34}$$

By multiplying both sides with $\cos[(2m+1)\theta]$ and then integrating this series equation in θ from 0 to π, we obtain linear equation set for x_m^j coefficients. After some algebra necessary to exclude the constants C^1 and C^2, two coupled infinite-matrix equations are cast into the following form:

$$x_m^j-\sum_{n=1}^{\infty}g_n^jx_n^jS_{m,n}(\theta_j)+\sum_{n=1}^{\infty}\gamma_n^kx_n^k\,T_{m,n}(\theta_j)=\sum_{n=1}^{\infty}n(n+1)p_n^jT_{m,n}(\theta_j)\quad \text{for } j=1,2,k=2,1 \tag{35}$$

where

$$S_{m,n}(x)=\frac{2}{\pi}\left[Q_{m,n}(x)-\frac{Q_{m,0}(x)\cdot Q_{0,n}(x)}{Q_{0,0}(x)}\right] \tag{36}$$

$$T_{m,n}(x)=\delta_{m,n}-S_{m,n}(x) \tag{37}$$

$$Q_{m,n}(x)=\frac{1}{2}\left[\frac{\sin((m+n+1)x)}{m+n+1}+\frac{\sin((m-n)x)}{m-n}\right] \tag{38}$$

with $\delta_{m,n}$ representing the Krönecker symbol.

Note that no numerical integration is needed to fill in the matrix in (35) that entails very fast algorithm in contrast to conventional MM codes. Now, collect all the unknowns into a single column vector $X=\{x_n^1,x_n^2\}_{n=1}^{+\infty}$ and all the right-hand parts into the known column vector B, which contains the characteristics of the probe. Furthermore, introduce the block-type (2×2) infinite matrix $A=\{A^{ps}\}_{p,s=1,2}$ built of four infinite blocks $A^{ps}=\{A_{mn}^{ps}\}_{m,n=1}^{+\infty}$ generated by (35) in obvious manner. Then (35) can be written in the following way:

$$X+AX=B. \tag{39}$$

Note that each matrix element is a product of two functions: $A_{mn}^{ps}=A_n^{ps(1)}(r_1,r_2,k_1,k_2,k_3,\eta_1,\eta_2,\eta_3)\cdot A_{mn}^{ps(2)}(\theta_1,\theta_2)$, the first of which goes to 0 if $k_3r_1\to0$ and $r_1/r_2\to0$, thus certifying that when building (39) we had inverted explicitly the static part of the problem associated with each spherical disk in free space.

Generally, studying the large-index behavior we find that

$$A_n^{ps(1)}=O(n^{-1}), A_{mn}^{ps(2)}=O[(m-n)^{-1}], A_{nn}^{ps(2)}=O(1). \tag{40}$$

Introducing the Hilbert space of square-summable number sequences $l_2^2=l_2\otimes l_2$ with the corresponding scalar product $(X_1X_2)=\sum_{n=1}^{\infty}(x_{n1}^1x_{n2}^1+x_{n1}^2x_{n2}^2)$, it is easy to see that $\|A\|_{l_2^2}<\infty$, therefore A is a completely continuous operator in l_2^2, hence it is compact [20]. Besides, $B\in l_2^2$. Therefore, (35) is a Fredholm second-kind matrix equation, or, in other words, (39) is a canonical Fredholm operator equation, whose unique solution belonging to l_2^2 is given by $X=(I+A)^{-1}\cdot B$. Moreover, the solution to the N-th order truncated equation given by $X^N=(I_{2N}+A^N)^{-1}\cdot B^N$, where each block of the 2×2 matrix A^N has the size $N\times N$, converges in the piecewise manner to the exact solution X, if $N\to\infty$ [8]. The last necessary step is to verify the edge condition (4). Inspection of the large-m behavior of A_{mn}^{ps} and B_m^p shows that it is determined by the functions (36) and (37) and given by $\mathrm{O}(m^{-1})$. Therefore, the solution of (35) satisfies (29) and hence (4), i.e., belongs to the sub-set of l_2^2 determined by the edge condition. This validates assumptions leading to (30).

IV. Antenna Characteristics

The shape of the far field is determined by the large-argument asymptotic behavior of the spherical Bessel and Hankel functions (see [21, p. 437]). For example

$$\vec{H} = \frac{E_0}{\eta_3}\frac{e^{-jk_3r}}{k_3r}\vec{\varphi}\sum_{n=1}^{\infty} j^n \alpha_n^{43} P_n^1(\cos\theta)(1+O(1/k_3r)). \quad (41)$$

Consequently, the far-field radiation pattern introduced in (3) is given by

$$f(\theta) = \sum_{n=1}^{\infty} j^n \frac{2n+1}{n(n+1)}\frac{x_n^2}{v_n} P_n^1(\cos\theta). \quad (42)$$

The radiated power P_r is given by the Poynting vector total flux through a distant sphere. Thanks to the orthogonality relation—see (19), it reduces to

$$P_r = 2\pi\frac{E_0^2}{\eta_3 k_3^2}\sum_{n=1}^{\infty}\frac{2n+1}{n(n+1)}\left|\frac{x_n^2}{v_n}\right|^2. \quad (43)$$

It is interesting to compare P_r with the power radiated by the same source (1) located in free space, that is

$$P_{\text{feed}} = (12\pi)^{-1}\eta_3|I_0|^2 k_3^2(r_2-r_1)^2. \quad (44)$$

The normalized value, P_r/P_{feed}, coincides with the normalized radiation (input) resistance of MSA. In the case of this value being greater, respectively lower, than the unity, the MSA conductors and spherical substrate improve, respectively deteriorate, the radiated power. Note that the same value, and also input reactance, can be found from the near field of antenna by using the Poynting theorem.

The directivity D of the antenna represents the ratio of the radiation intensity in a given direction to this value averaged over all directions [21]. In our case, this yields

$$D(\theta) = \frac{2\pi E_0^2}{\eta_3 k_3^2 P_r}\left|\sum_{n=1}^{\infty} j^n \frac{2n+1}{n(n+1)}\frac{x_n^2}{v_n}P_n^1(\cos\theta)\right|^2. \quad (45)$$

The electrical current on each disk is obtained as a jump in the tangential magnetic field across its surface. In the terms of series, this is given by

$$\vec{J}_s(\theta) = j\cdot E_0\vec{\theta}\cdot\sum_{n=1}^{\infty} P_n^1(\cos\theta)\cdot\left[\eta_2^{-1}\alpha_n^{t2}\cdot Z_n^t(k_2r_s) + \eta_2^{-1}\left(\alpha_n^{q2}+\beta_n^{\text{it}}\right)\cdot Z_n^q(k_2r_s) - \eta_p^{-1}\alpha_n^{qp}\cdot Z_n^1(k_pr_s)\right] \quad (46)$$

where for $s=1$ we imply $t=4, q=1$, and $p=1$, while for $s=2$ we have $t=1, q=4$, and $p=3$.

V. Numerical Results

Now we shall present some numerical results in order to illustrate the influence of two major MSA parameters: the size of the ground and the curvature. However, at first we show the relative error $e_r(N)$ associated with the truncation of each block of the matrix. This quantity is defined as

$$e_r(N) = \frac{\|X^N - X^{N-1}\|_{l_2^2}}{\|X^N\|_{l_2^2}}. \quad (47)$$

It shows the normalized difference between two adjacent-N solutions of the matrix equation. Typical behavior of $e_r(N)$ is shown in Fig. 2. For large values of N, this quantity behaves like $(r_1/r_2)^N$. All the further computations were done with $N=120$, except for the plots in Fig. 4, where we took $N=150$. The choice of this value is clear from Fig. 2 and ensures a 3-digit accuracy in solving the matrix, for the considered normalized frequencies and fixed $r_1/r_2 = 0.97$.

Fig. 3 presents the relief of P_r/P_{feed} as a function of two parameters: ground size and normalized frequency. It shows that if $\theta_1 > \theta_2$, the resonance frequencies and the radiated power are fixed. However, if the inner disk becomes smaller than the outer one, the resonance frequencies grow up, while their Q-factors and hence the radiated power falls down.

The plot in Fig. 4 corresponds to a cut of the relief in Fig. 3, i.e., to the case of an incomplete spherical ground conductor ($\theta_1 = 160^\circ$). The values of the first several resonance frequencies of the patch are marked here. As explained before, these values do not change significantly when the inner conductor is a finite-size disk greater than the outer one. In the high-frequency part of the plot one can see periodic small-amplitude ripples caused by the spherical-substrate waves, which travel around the spherical ground like the whispering-gallery modes. Besides, one can notice the presence of a low-Q resonance close to $k_3r_2 = 1$. This is the resonance of the spherical ground itself. To emphasize this effect, the dotted and dashed curves in Fig. 4 show the same dependence in the case of a bare and coated PEC sphere, respectively, fed by the coaxial probe.

The far-field radiation patterns and the current distribution on the metallic disks associated to the marked normalized frequencies are plotted in Fig. 5. This shows that the currents on the inner and the outer conductors are almost the same. Moreover, on the ground disk, the current distribution decreases smoothly when crossing the angular position, which corresponds to the rim of the patch disk. In addition to this, one can observe that the nth resonance frequency is associated with n variations in the patch-disk current magnitude from its pole to the rim. As here the separation (substrate thickness), $r_2 - r_1$, is smaller than half-wavelength in the dielectric of $\varepsilon_r = 1.3$ for the normalized frequencies up to k_3. r_2 =50, there is no variation of the resonant E-field between the disks for any of significant resonances. Therefore, these frequencies are associated with the TM_{0n0} resonance modes. Besides, each TM_{0n0} mode has the far field pattern whose number of lobes in the forward half-space is also n. The greater the normalized frequency, the greater the backward radiation and the narrower the main beam. If the frequency is very large, then the most intensive beam radiates backward-this "keel-over" effect has been earlier reported for a conventional spherical-circular MSA [9].

In addition to this, Fig. 6 shows the dependence of the maximum directivity on the frequency. It is slightly improved by the presence of the ground surface. It can be also noted that the directivity is very similar in all the cases when the ground surface is greater than the patch, except of the "keel-over" band. The main-beam direction varies with the frequency, as shown in Fig. 7, and eventually displays a "keel-over." Its nature is entirely explained by the waveguide features of the spherical dielectric substrate that dominate over the patch effect if the frequency or substrate thickness is large. However, by

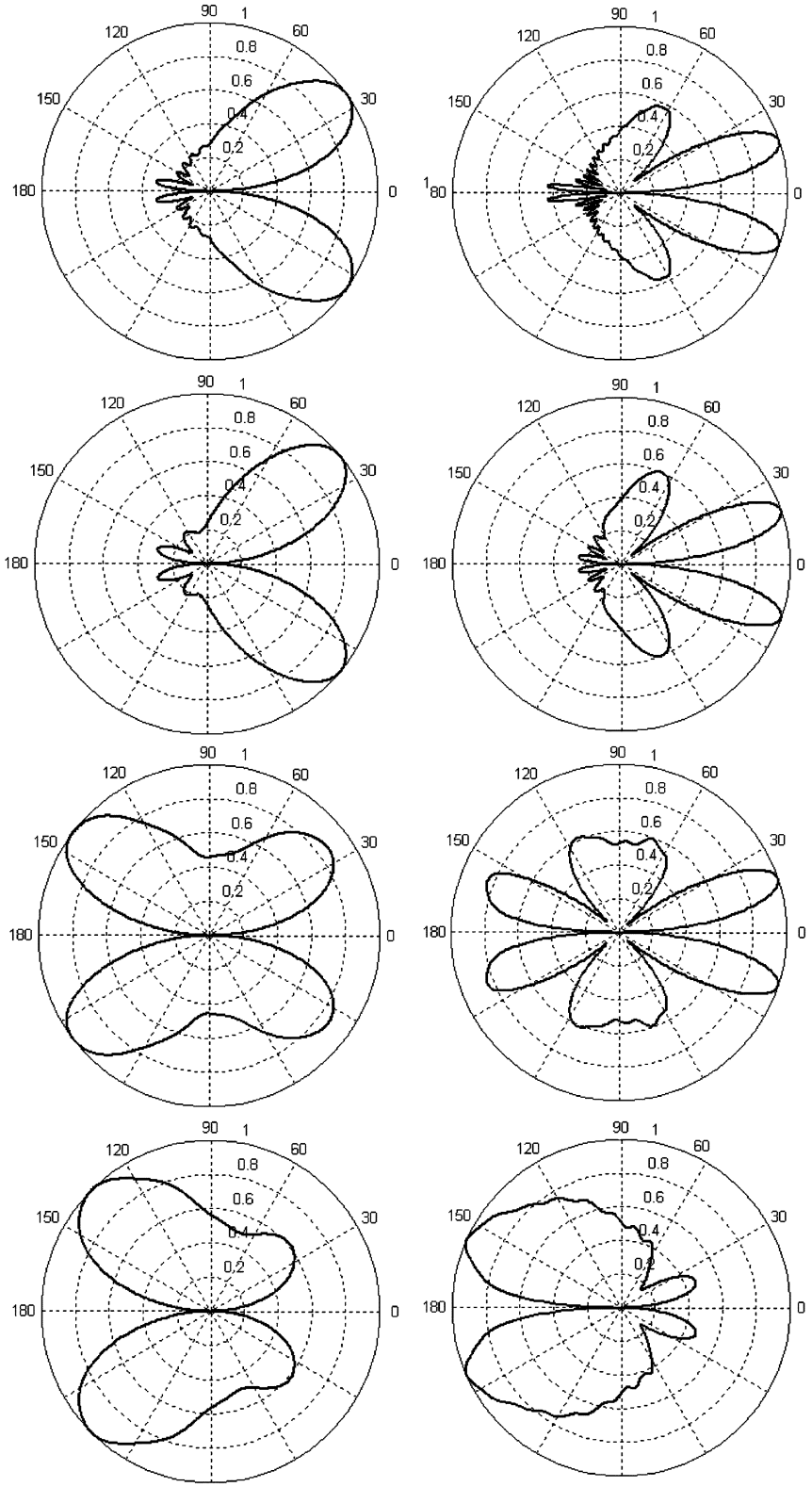

Fig. 8. Influence of the ground size on the far field pattern in the maxima ($kr_2 = 9.95$ for the left column, $kr_2 = 18.41$ for the right one) of the radiated power at $\theta_1 = 180°$. $\theta_2 = 18°, r_1/r_2 = 0.97, \varepsilon_{r1} = \varepsilon_{r3} = 1, \varepsilon_{r2} = 1.3$. From top to bottom, the values of the ground size are $\theta_1 = 180°, 40°, 18°$, and $0°$.

placing a patch over the feed, one can shift the "keel-over" frequency to a much higher value.

In order to emphasize these remarks on the ground size effect, Fig. 8 exposes modifications of the radiated far-field pattern at the first two resonances of MSA with a spherical ground. So far as $\theta_1 > \theta_2$, the pattern does not change significantly. However, in the case of equal angular sizes of the two metallic disks, the backward and the forward-radiated field patterns are very similar to each other. If the inner metallic disk becomes smaller than the outer one, the orientation of the radiated far-field pattern is

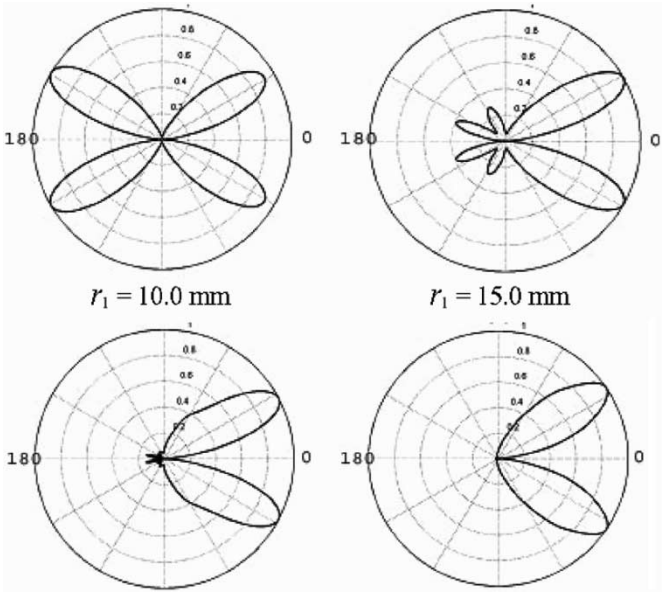

Fig. 9. Influence of the radius of curvature on the far-field pattern at 9.95 GHz. $\theta_1 = 180°, \theta_2 \cdot r_2 = 15$ mm, $r_2 - r_1 = 1.4$ mm, $\varepsilon_{r1} = \varepsilon_{r3} = 1, \varepsilon_{r2} = 1.3$.

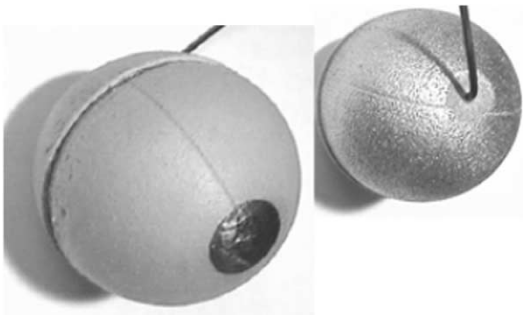

Fig. 10. Conformal antenna used in comparison of theory with experiment: front side view (left) and back side view (right). The slot separating foam hemispheres and the feeding cable are visible.

inverted. Then, the inner disk behaves like a patch and the outer one like a ground.

Consequently, the main conclusion of these observations is that the smaller-size metallic conductor determines the resonant frequency. That is why the ground size is a very important parameter for such conformal printed antennas.

The influence of the radius of curvature of the MSA with the spherical ground is shown in Fig. 9. Here, the curvilinear radius of the patch is a fixed value, $\theta_2 r_2 = \text{const}$, and $k_3\sqrt{\varepsilon_{r2}}\theta_2 r_2 = 3.832$, that corresponds to the "cavity-model" TM_{010} resonance of a flat circular-disk MSA [21]. However, such a "first guess" value happens to be pretty far off the resonance for our MSA on the spherical substrate, until its radius is $r_1 < 35.0$ mm. This is well observable from the radiation pattern shape. Shifting the resonance frequency to the required 10 GHz occurs at $r_1 = 35$ mm. In this case, the pattern shape is close to the ones given previously. A more interesting situation corresponds to $r_1 > 35$ mm. Here the influence of the substrate curvature variation is smaller, hence the TM_{010} resonant frequency is almost fixed and the far-field pattern variations are minor. The greater the radius of curvature, the closer the radiation pattern to that of a flat circular MSA backed with infinite PEC ground plane.

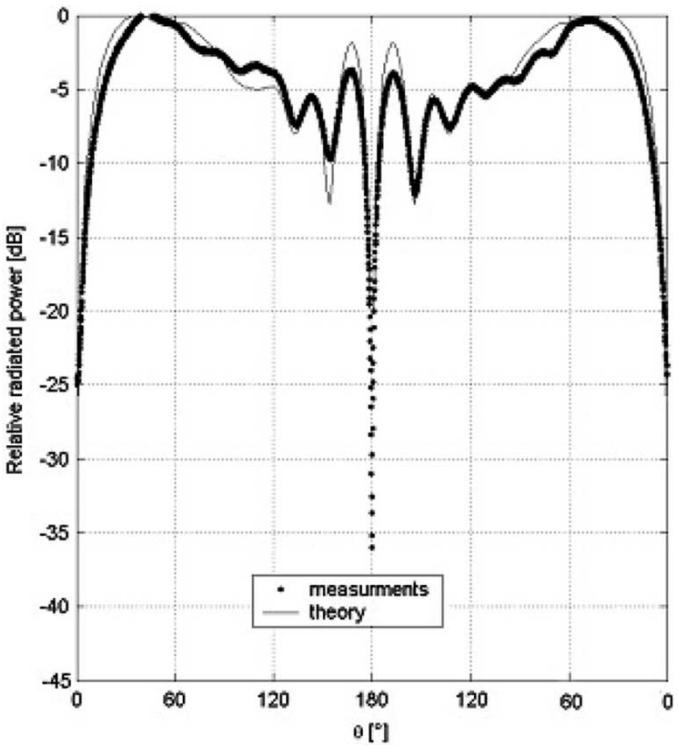

Fig. 11. Comparison between the measurements and theory for the radiated far field at 9 GHz. $\theta_1 = 160°, \theta_2 = 16°, r_1 = 35$ mm, $r_2 = 38$ mm, $\varepsilon_{r1} = \varepsilon_{r3} = 1.23, \varepsilon_{r3} = 1$.

VI. Validation

Partial validation of our results has been done by recreating the conditions studied in [9], i.e., by considering a spherical-circular MSA with a spherical PEC ground excited by elementary RED of the length $l \to 0$. This needs replacing unit-function r-dependence of the driving current density in (1) with the Dirac-delta factor $l\delta(r)$ and other relevant simple modifications. The equations obtained in this case coincide with those of [9]. Besides, we have computed an input resistance scan in frequency with HFSS 8 commercial solver: it took 16 hrs 41 min using 41 389 cells against 1 s with MAR using 150 unknowns.

In order to see the accuracy of simulation, a conformal printed antenna was manufactured (see Fig. 10) and measured. It had a metalized foam substrate (see [22], [23]), whose technology is controlled by the University of Rennes I. Two hemispherical foam caps were placed on a copper sphere having a hole for the coaxial-cable feeder. The feeder was piercing the foam and contacting a smaller disk patch deposited at the pole opposite to the feed hole. Electromagnetic and geometrical parameters of this antenna are as follows: $\theta_1 = 160°, \theta_2 = 16°, r_1 = 35$ mm, $r_2 = 38$ mm, $\varepsilon_{r1} = \varepsilon_{r3} = 1.23, \varepsilon_{r3} = 1$. Numerous measurements have been carried out; a typical example is given in Fig. 11 and relates to the frequency of 9 GHz. All the other measurements were in similar excellent agreement with theoretical results. A few discrepancies are due to some difficulties of positioning the sphere in the anechoic chamber and certain perturbation caused by the feeding coaxial cable.

VII. Conclusion

The presented analysis shows that MAR is a powerful and efficient analytical-numerical method dealing with a global field

computation. Indeed, the separation in terms of direct field—reflected field—diffracted field is not so convenient here as it is in high-frequency methods such as GTD or PTD. More adequate physical interpretation of the results is achieved in terms of action (radiation of the feeding probe) and reaction (influence of the scattering structures).

Unlike previous studies, here we expanded electromagnetic field in terms of the spherical vector wave modes and assumed finite size of the ground surface. Computations have shown that the angular size of the ground and its radius of curvature are, in some cases, critical parameters, which must be properly taken into account. The MAR method allows analyzing more complicated stacked structures, such as conformal spherical patch with a similar parasite and finite-size ground surface, excited by the centered radial and tangential dipoles simulating probe and slot feeding. Arbitrarily positioned probe excitation, although treatable, presents a more complicated problem as it generates infinite number of the azimuth field harmonics. Another interesting research problem is simulation of a Lüneburg lens antenna fed by a circular-spherical MSA.

ACKNOWLEDGMENT

The authors wish to thank J. Sorieux, technician at the University of Rennes I, for the high quality of realization of antennas used in the experimental validation. A. I. Nosich and S. S. Vinogradov are grateful to the same university for the visiting opportunities.

REFERENCES

[1] B. Ke and A. A. Kishk, "Analysis of spherical circular microstrip antennas," *Proc. Inst. Elect. Eng.*, pt. H, vol. 138, pp. 542–548, 1991.

[2] K.-L. Wong, S.-F. Hsiao, and H.-T. Chen, "Resonances and radiation of a superstrate-loaded spherical-circular microstrip patch antenna," *IEEE Trans. Antennas. Propagat.*, vol. 41, pp. 686–690, May 1993.

[3] A. A. Kishk, "Analysis of a spherical annular microstrip antenna," *IEEE Trans. Antennas. Propagat.*, vol. 41, pp. 338–343, Mar. 1993.

[4] T.-T. Chen, H.-D. Chen, and Y.-T. Cheng, "Full-wave analysis of the annular-ring loaded spherical-circular microstrip antenna," *IEEE Trans. Antennas Propagat.*, vol. 45, pp. 1581–1583, Nov. 1997.

[5] K.-L. Wong, *Design of Nonplanar Microstrip Antennas and Transmission Lines*. New York: Wiley, 1999.

[6] D. G. Dudley, "Error minimization and convergence in numerical methods," *Electromagn.*, vol. 5, no. 2–3, pp. 89–97, 1985.

[7] G. L. Hower, R. G. Olsen, J. D. Earls, and J. B. Schneider, "Inaccuracies in numerical calculation of scattering near natural frequencies of penetrable objects," *IEEE Trans. Antennas Propagat.*, vol. 41, pp. 982–986, July 1993.

[8] A. I. Nosich, "The method of analytical regularization in wave-scattering and eigenvalue problems: Foundations and review of solutions," *IEEE Antennas Propagat. Mag.*, vol. 41, pp. 25–49, June 1999.

[9] V. V. Radchenko, A. I. Nosich, S. S. Vinogradov, and J.-P. Daniel, "A conformal spherical-circular microstrip antenna: Axisymmetric excitation by an electric dipole," *Microwave Opt. Technol. Lett.*, vol. 26, no. 3, pp. 176–182, 2000.

[10] S. S. Vinogradov, "A soft spherical cap in the field of a plane sound wave," *U.S.S.R. J. Math. Phys. Computat. Math. (English Translation)*, vol. 18, no. 5, pp. 244–249, 1978.

[11] ——, "Reflectivity of a spherical shield," *Radiophys. Quantum Electron. (English Translation)*, vol. 26, no. 1, pp. 78–88, 1983.

[12] R. W. Ziolkowski, D. P. Marsland, L. F. Libelo, and G. E. Pisane, "Scattering from an open spherical shell having a circular aperture and enclosing a concentric dielectric sphere," *IEEE Trans. Antennas Propagat.*, vol. 36, pp. 985–999, July 1988.

[13] S. S. Vinogradov, E. D. Vinogradova, A. I. Nosich, and A. Altintas, "Analytical regularization based analysis of a spherical reflector symmetrically illuminated by an acoustic beam," *J. Acoust. Soc. Amer.*, vol. 107, no. 6, pp. 2999–3005, 2000.

[14] L. Economou and R. J. Langley, "Patch antenna equivalent to simple monopole," *Electron. Lett.*, vol. 33, no. 9, pp. 727–728, 1997.

[15] Y. J. Guo, A. Paez, R. A. Sadeghzadeh, and S. K. Barton, "A circular patch antenna for radio LANs," *IEEE Trans. Antennas Propagat.*, vol. 45, pp. 177–178, Jan. 1997.

[16] A. G. Pino, A. M. Arias-Acuna, and J. O. Rubinos-Lopez, "An omni-directional dual-shaped reflector antenna," *Microwave Opt. Technol. Lett.*, vol. 27, no. 5, pp. 371–374, 2000.

[17] D. Colton and R. Kress, *Integral Equation Methods in Scattering Theory*. New York: Wiley, 1983, ch. 4.

[18] J. A. Stratton, *Electromagnetic Theory*. New York: McGraw-Hill, 1941.

[19] *Handbook of Mathematical Functions*, M. Abramowitz and I. A. Stegun, Eds., Dover, New York, 1985, p. 338.

[20] N. I. Akhiezer and I. M. Glazman, *Theory of Linear Operators in Hilbert Space*. New York: Fr. Ungar, 1961.

[21] C. A. Balanis, *Antenna Theory: Analysis and Design*, 2nd ed. New York: Wiley, 1997, p. 39.

[22] M. Himdi, S. Chainon, and J.-P. Daniel, "Technologie d'antennes 2D et 3D en mousse métallisée," in *Proc. SEE 2001*, Paris, France, 2001, pp. 99–104.

[23] B. Jecko, F. Jecko, M. Himdi, and J.-P. Daniel, "Design and technologies of 2D and 3D antennas from L-band up to V-band," in *Proc. Int. Symp. Antennas Propagation (ISAP 2000)*, Fukuoka, Japan, 2000.

Sébastien Rondineau was born in Paimboeuf, France, in 1975. He received the "Diplôme d'Ingénieur en Informatique et téléCommunications," the Postgraduate degree in signal processing and telecommunications, in 1999 and the Ph.D. degree in 2002 from the University of Rennes 1, France.

Currently, he is a Research Associate at the Microwave and Active Antenna Laboratory of the Electrical and Computer Engineering Department, University of Colorado at Boulder. His research interests include the method of analytical regularization in computational electromagnetics, propagation and scattering of waves, dielectric lenses, discrete lens arrays, and antennas.

Alexander I. Nosich (M'94–SM'95) was born in Kharkov, Ukraine, in 1953. He received the M.S., Ph.D., and D.Sc. degrees, all in radio physics, from the Kharkov National University in 1975, 1979, and 1990, respectively.

Since 1979, he has been on Research Staff of the Institute of Radio-Physics and Electronics of the National Academy of Sciences of Ukraine in Kharkov. Currently, he holds a post of a Leading Scientist and heads a research group. From 1992 to 2003, he held a number of guest fellowships and professorships in Turkey, Japan, Italy, France, Spain, and Singapore. His research interests include the method of analytical regularization in computational electromagnetics, propagation and scattering of waves, modeling of lasers, open waveguides, and antennas, and the history of microwaves. From 1990 to 2002, he was one of initiators and technical program committee chairman of the series of international conferences on mathematical methods in electromagnetic theory (MMET) in the U.S.S.R. and Ukraine. In 1995, he was the organizer of the IEEE Antennas and Propagation Society Chapter in East Ukraine, the first one in the former U.S.S.R. (now joint chapter with IEEE MTT, AES, EDS, GRS, NPS, and EMB Societies). From 2001 to 2003, he was an appointed Member of the European Microwave Association representing Ukraine, Poland, and the Baltic states.

Jean-Pierre Daniel, photograph and biography not available at the time of publication.

Mohamed Himdi, photograph and biography not available at the time of publication.

Sergei S. Vinogradov, photograph and biography not available at the time of publication.